Multiple-Zone Strategy for Supersonic Missiles

Andrew B. Wardlaw Jr.,* Francis J. Priolo,† and Jay M. Solomon‡
Naval Surface Weapons Center, White Oak, Silver Spring, Maryland

A multiple-zone computational method applicable to finned bodies in supersonic flight is described. At each cross section, the computational domain is broken into a number of zones, each of which can be described using a simple mapping. The zones are chosen to ensure that the bow shock and fin and body surfaces coincide with zone edges. At zone interfaces, the mesh may be discontinuous in a direction normal to the edge. Along zone edges, surfaces are allowed to form or disappear during the computation. The surface edges that form at points where surfaces appear or disappear are treated using a local analysis. Calculations are performed for several complex missile configurations. In general, computational results are in good agreement with experimental data.

Nomenclature

A_c = reference area
$b(\phi, \bar{z}), c(\phi, \bar{z})$ = radial location of edges 1 and 3, respectively (see Fig. 3)
C_N = normal force coefficient (normal force)/$(A_c q_\infty)$
C_{ML} = rolling moment coefficient (rolling moment)/$(A_c q_\infty D)$
D = diameter
j = $x_\xi y_\eta - x_\eta y_\xi$
J = $\xi_x \eta_y - \xi_y \eta_x$
p = pressure
q_∞ = dynamic pressure
Z_{cp} = center of pressure
$(r, \phi, \bar{z})$ = cylindrical coordinates (see Fig. 1)
(u, v, w) = Cartesian velocity components (see Fig. 1)
V = $\alpha_x v + \alpha_y u$
(x, y, z) = Cartesian coordinates (see Fig. 1)
α = angle of attack
(α, β, γ) = surface-oriented computational coordinates; $\alpha = 0$ located along surface
(ξ, η, ζ) = computational coordinates (see Fig. 3)
ρ = density
$\sigma(r, \bar{z}), \psi(r, \bar{z})$ = angular locations of edges 4 and 2, respectively

I. Introduction

In supersonic flow, the Euler equations can be numerically solved using a marching procedure that starts from an initial-data plane near the missile nose. A major problem encountered is the treatment of complex cross-sectional geometries that arise in conjunction with configurations featuring fins, inlets, and tails. Most inviscid treatments [1-7] for arbitrary bodies employ a wraparound transformation that maps both the body and fin surfaces onto an edge of the computational region as shown in Fig. 1a. Mapping methods have been developed for arbitrary configurations,[2] including bodies with wings. However, for missiles with multiple wings and fins that are thin and have sharp edges, this type of approach has several drawbacks. A significant portion of the computation may be associated with constructing the mesh-generating transformation. Also, solutions may be sensitive to small changes in the transformation, and it is often difficult to control mesh spacing throughout the flowfield.

An alternative approach for treating complex missile and aircraft configurations is a multiple-zone strategy. Here the computational domain in every cross section is divided into several zones, each of which can be treated using a simple mapping. This avoids many of the mapping complexities associated with wraparound meshes; however, it introduces additional program complexity associated with interconnecting adjacent zones. Despite these difficulties, the multiple-zone method described in this paper is capable of treating a wider variety of configurations than a wraparound mesh method. Furthermore, use of a separate mesh in each zone allows selected portions of the flowfield to be resolved in greater detail.

Multiple-zone methods have been used in applications of the unsteady Euler equations to a number of complex configurations including inlets with blunt lips,[8] airfoils with flaps,[9] and body-wing combinations.[10] In these studies, two basic multiple-zone structures have been used: overlapping zones or abutting zones that interface only along a common boundary. Regardless of the type of zone interface employed, information is transmitted between adjacent zones by interpolation. If shocks are to be captured, this interpolation procedure should preserve the global conservation properties of the scheme (see, e.g., Ref. 11).

This paper focuses on the application of a multiple-zone approach to missiles and aircraft with thin, sharp fins or wings. Such shapes are conveniently treated using abutting zones, with portions of the boundaries taken to coincide with segments of the body, fin, or tail surface, and the bow shock. Since the cross-sectional geometry and bow shock location vary along the missile axis, the transformation in each zone must be recomputed at every step in the calculation. To promote efficiency, simple analytic mappings are used. The complexity of the interfacing algorithm is reduced by requiring that points along adjacent zone boundaries be coincident. This allows the application of an edge-point treatment that does not require interpolations while preserving a global conservation property. The mesh spacing normal to the zone edge may be discontinuous; however, this may have an adverse effect on the solution accuracy. Each zone is advanced using the explicit MacCormack scheme with wall and shock points being treated by characteristic analysis. Special computational methods are applied at corners, body-fin junctures, surface edges, and surface slope discontinuities.

Section II of this paper describes zone structure and linking, while the numerical techniques are outlined in Sec. III. A more detailed description of the numerical technique can be found in Ref. 12. Results for several missile shapes are presented in Sec. IV, and concluding remarks are presented in Sec. V.

Received Jan. 13, 1986; revision received July 22, 1986.

*Aerospace Engineer, Applied Mathematics Branch. Associate Fellow AIAA.
†Aerospace Engineer, Applied Mathematics Branch. Member AIAA.
‡Mathematician, Applied Mathematics Branch. Member AIAA.

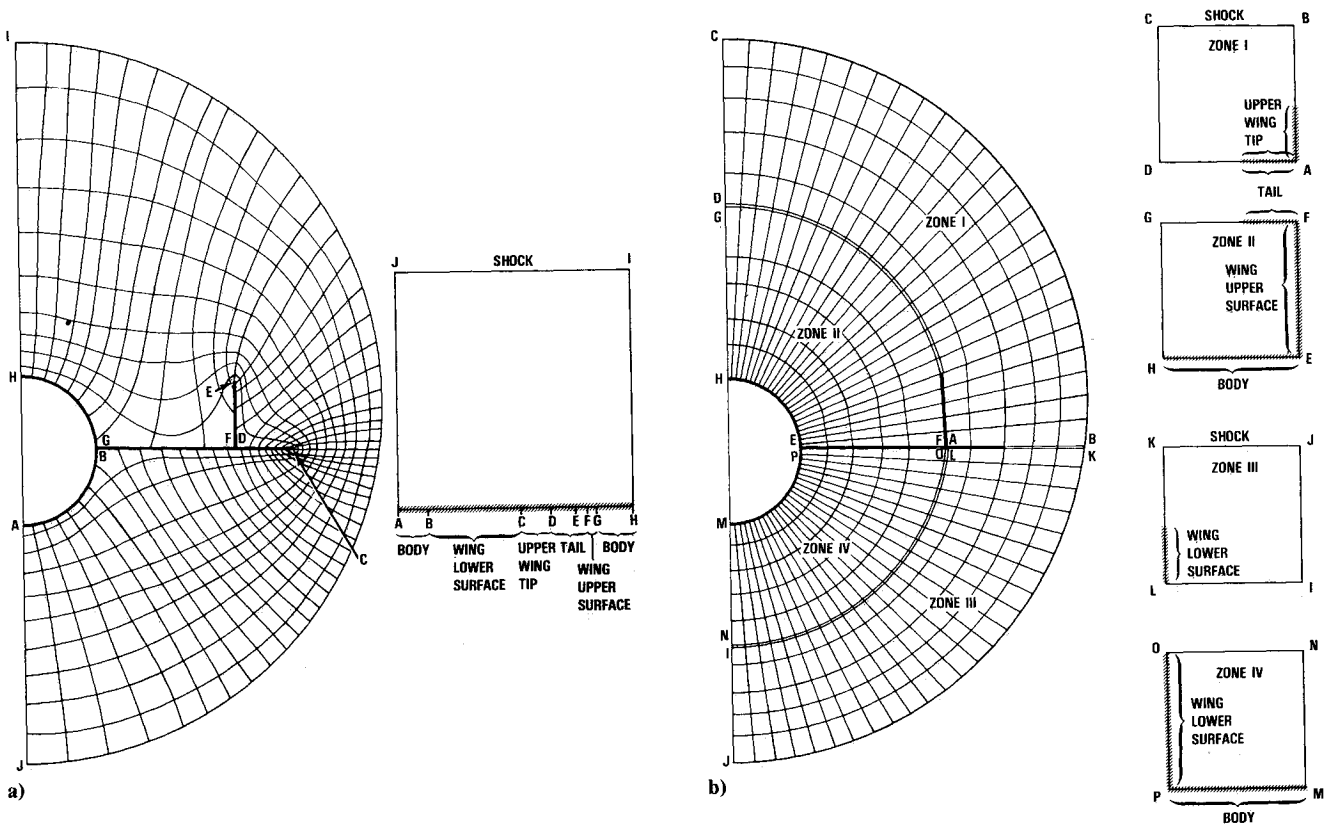

Fig. 1 Different mesh types: a) wraparound, b) multiple zone.

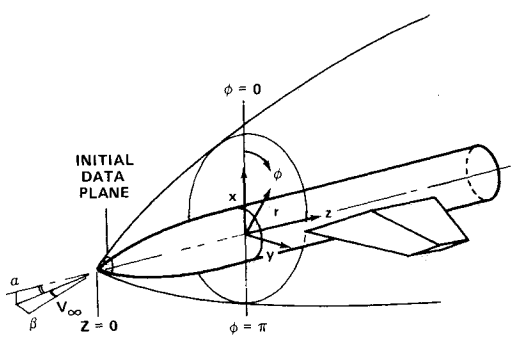

Fig. 2 Cartesian and cylindrical coordinate systems.

II. Multiple-Zone Methodology

The multiple-zone procedure is implemented by dividing the shock layer into nonoverlapping, quadrilateral zones. Zone edges are taken to coincide with walls and the bow shock, if one exists. Here a wall refers to any surface at which a tangent-flow boundary condition is applied, such as body, fin, or tail surfaces. Points interior to the shock layer may also lie on zone edges. Juncture points, which are the intersection of two wall surfaces, must occur at zone corners. Points lying on zone edges may change their type at different axial stations from interior to wall, and vice versa. Similar transitions between interior, wall, and juncture points can also occur at a zone corner. This allows the simulation of inlet lips and wings with leading and trailing edges. In the present procedure, the intent is to fit the bow shock as a boundary for the computational domain and to let the conservative properties of the difference scheme capture all other (embedded) shocks. Figure 1b illustrates an example of a four-zone model at a cross section featuring a body, wing, and tail.

All interior points are governed by the steady Euler equations, which are cast in the Cartesian coordinates (x, y, z) defined in Fig. 2. In each zone, these equations are transformed to computational space (ξ, η, ζ) using the mapping described in the next subsection. The transformed equations for each zone, are written in conservation form as

$$\frac{\partial U}{\partial \zeta} + \frac{\partial F}{\partial \xi} + \frac{\partial G}{\partial \eta} = 0 \tag{1}$$

where

$$U = (\hat{U}/J),\ F = (\xi_z \hat{U} + \xi_x \hat{F} + \xi_y \hat{G})/J$$

$$G = (\eta_z \hat{U} + \eta_x \hat{F} + \eta_y \hat{G})/J,\ J = \xi_x \eta_y - \xi_y \eta_x$$

$$\hat{U} = \begin{bmatrix} \rho w \\ p + \rho w^2 \\ \rho uw \\ \rho vw \end{bmatrix},\quad \hat{F} = \begin{bmatrix} \rho u \\ \rho uw \\ p + \rho u^2 \\ \rho vu \end{bmatrix},\quad \hat{G} = \begin{bmatrix} \rho v \\ \rho vw \\ \rho vu \\ p + \rho v^2 \end{bmatrix}$$

A different set of computational coordinates is used in each zone.

Zone Description

In the cross-flow planes ($z = \text{const}$), zones are generalized quadrilaterals as shown in Fig. 3. Each zone is described with respect to a local cylindrical coordinate system $(r, \phi, \bar{z})$ with origin (x_0, y_0). This origin can be different for each zone, and its location may vary with $\bar{z}$. The use of cylindrical coordinates facilitates treatment of bodies that are typical of missiles. The numbering system used to designate the edges and corners of a zone is indicated in Fig. 3. The radial location of edges 1 and 3 are defined by the functions $b(\phi, \bar{z})$ and $c(\phi, \bar{z})$; the angular position of edges 2 and 4 are defined by $\psi(r, \bar{z})$ and $\sigma(r, \bar{z})$. In cases where a bow shock is fitted, the shock must be located on edge 3.

The mesh in each zone is defined by the transformation T_2T_1, where T_1: $(\xi, \eta, \zeta) \rightarrow (r, \phi, \bar{z})$ and T_2: $(r, \phi, \bar{z}) \rightarrow (x, y, z)$.

T_2 is given by

$$x = r\cos(\phi) + x_0(\bar{z})$$
$$y = r\sin(\phi) + y_0(\bar{z})$$
$$z = \bar{z}$$

while T_1 is defined as

$$r = b(\phi', \zeta) + [c(\phi'', \zeta) - b(\phi', \zeta)]f(\xi)$$
$$\phi = \sigma(r', \zeta) + [\psi(r'', \zeta) - \sigma(r', \zeta)]g(\eta)$$
$$z = \zeta \qquad (2)$$

where

$$\phi' = \phi_4(\zeta) + [\phi_1(\zeta) - \phi_4(\zeta)]g(\eta)$$
$$\phi'' = \phi_3(\zeta) + [\phi_2(\zeta) - \phi_3(\zeta)]g(\eta)$$
$$r' = r_4(\zeta) + [r_3(\zeta) - r_4(\zeta)]f(\xi)$$
$$r'' = r_1(\zeta) + [r_2(\zeta) - r_1(\zeta)]f(\xi)$$

and (r_i, ϕ_i), $i = 1, 2, 3, 4$ are the coordinates of the corners. Here f and g are mesh clustering functions with $f(0) = g(0) = 0$ and $f(1) = g(1) = 1$. In computational coordinates, the computational domain for each zone is bounded by $0 \le \xi \le 1$, $0 \le \eta \le 1$ and $\zeta \ge 0$.

The metric quantities $\xi_x, \xi_y, \xi_z, \eta_x, \eta_y, \eta_z$, appearing in Eqs. (1) are related to the derivatives of T_2T_1 as follows:

$$\xi_x = y_\eta/j, \quad \xi_y = -x_\eta/j, \quad \xi_z = -\xi_x x_\zeta - \xi_y y_\zeta$$
$$\eta_x = -y_\xi/j, \quad \eta_y = x_\xi/j, \quad \eta_z = -\eta_x x_\zeta - \eta_y y_\zeta \qquad (3)$$

where $j = x_\xi y_\eta - x_\eta y_\xi$. Except at edge points that link adjacent zones, the quantities $x_\xi, x_\eta, x_\zeta, y_\xi, y_\eta, y_\zeta$ can be determined either by central differencing or analytically, using the derivatives of T_1 and T_2. The treatment of interior points on zone edges is discussed below.

Zone Linking

Information must be passed between zones connected by abutting edges. Two edges are abutting if they possess segments containing points that are coincident in Cartesian space and not separated by a zero thickness surface. To simplify the interfacing scheme, the zones are defined to ensure that abutting edges satisfy the following rules:

1) The two sets of points on each of the abutting edge segments must be coincident in Cartesian space.

2) Odd-numbered zone edges must abut to odd-numbered edges and even to even. Also, edges with the same number cannot abut.

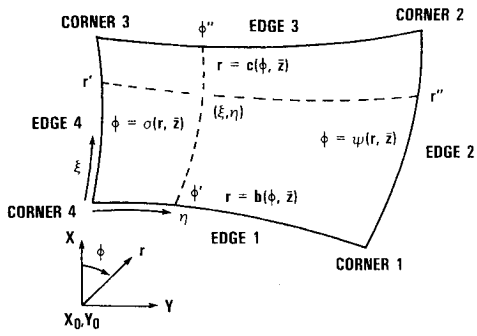

Fig. 3 Zone structure.

3) A zone corner on an abutting edge segment can be coincident in Cartesian space only with other zone corners.

Rule 1 requires that meshes in zones that abut produce coincident grid points in Cartesian space along the abutting edge segments. Restrictions are not imposed on the mesh spacing normal to abutting edges, and abrupt changes in mesh size can occur.

The computational algorithm treats each zone separately, except along abutting edges. Here flow properties and metric quantities from the abutting zones must be used. Appropriate metrics are defined by viewing the computational spaces of the abutting zones as a single, extended computational space. For example, consider the case of two abutting zones, I and II, with computational spaces (ξ', η', ζ') and (ξ'', η'', ζ''), respectively, and apply the discontinuous transformation:

$$\xi = \{\xi' \text{ in zone I}, a\xi'' + c_0 \text{ in zone II}\}$$
$$\eta = \{\eta' \text{ in zone I}, b\eta'' + c_1 \text{ in zone II}\}$$
$$\zeta = \{\zeta' \text{ in zone I}, \zeta'' \text{ in zone II}\}$$

where $a = \Delta\xi'/\Delta\xi''$, $b = \Delta\eta'/\Delta\eta''$. The constants c_0 and c_1 can be chosen so that the two zones correspond in the extended computational space (ξ, η, ζ) to a square and a rectangle joined along the abutting edge. Rule 1 implies that the combined mesh is continuous along the abutting edge and has a uniform spacing $\Delta\xi$, $\Delta\eta$ in the (ξ, η, ζ) space. Although x_ζ and y_ζ are continuous along the abutting edge, $x_\xi, x_\eta, y_\xi, y_\eta$ may be discontinuous. The discontinuities are removed in the present procedure by defining single values for these derivatives using standard centered differences in the ξ, η variables. Then, along the abutting edge,

$$x'_\xi = x''_\xi/a = \bar{x}_\xi, \; x'_\eta = x''_\eta/b = \bar{x}_\eta$$
$$y'_\xi = y''_\xi/a = \bar{y}_\xi, \; y'_\eta = y''_\eta/b = \bar{y}_\eta$$

where the overbar denotes values from the centered differences. The required metric quantities $\xi_x, \xi_y, \xi_z, \eta_x, \eta_y, \eta_z$ then follow from Eq. (3). As will be shown in Sec. III, the above modifications to the metrics at abutting edges permits the application of the MacCormack scheme with only slight modification. Interpolation is not required, and the scheme satisfies a global conservation property such as that of Ref. 11.

The use of central differences to calculate metrics along abutting edges is consistent with a second-order accurate scheme when the mesh variation across the abutting edge is sufficiently smooth in Cartesian space. In other cases, a degeneration in accuracy probably occurs. In Ref. 13, the present method was applied to flow over biconics using two zones that featured a 5:1 jump in mesh spacing across the abutting edge. When the zone edge was in a smooth flow region, the resulting solution was in close agreement with results obtained using a single uniform mesh. In cases where a shock wave crossed the abutting edges, the shock trajectory was accurately captured in both zones, but additional numerical noise was introduced on the downstream side of the shock.

III. Numerical Procedures

The solution in each zone is advanced in its own computational space. A common marching step size is employed in all zones, which is determined by applying the CFL condition to all points in the calculation. In the following, the numerical procedures are briefly outlined. A more detailed description can be found in Refs. 12 and 14.

Interior Points

Interior points are advanced using the explicit MacCormack scheme applied to Eqs. (1). The same variant of this scheme (i.e., forward-backward or backward-forward) is applied to each zone. At interior points lying on an abutting edge, this

scheme must be modified to allow access to the information in the abutting zones. This is accomplished by viewing the abutting zones as part of an extended computational space, as was done in Sec. II. In the extended space, Eqs. (1) holds both in and on the edges of the abutting zones. The metric treatment of Sec. II provides a continuous definition of the metric quantities and the fluxes U, F, G in the neighborhood of the abutting edges. This allows, in the extended space, the MacCormack scheme to be applied in the standard manner at points located along the abutting edge. The predictor and corrector formulas for the extended space are then converted to the individual zone spaces to obtain the predictor and corrector formulas for the edge points in each zone. For example, in the case of two abutting zones discussed in Sec. II, this conversion is obtained as follows:

$$\Delta\xi = \{\Delta\xi' \text{ in zone I}, a\Delta\xi'' \text{ in zone II}\}$$

$$\Delta\eta = \{\Delta\eta' \text{ in zone I}, b\Delta\eta'' \text{ in zone II}\}$$

$$U = \left\{U' \text{ in zone I}, \frac{U''}{ab} \text{ in zone II}\right\}$$

$$G = \left\{G' \text{ in zone I}, \frac{G''}{a} \text{ in zone II}\right\}$$

$$F = \left\{F' \text{ in zone I}, \frac{F''}{b} \text{ in zone II}\right\}$$

Here prime and double prime signs denote quantities evaluated in zone I and II computational spaces, respectively. The above procedure ensures that the decoded flow variables at the abutting edge points in each zone are identical for both the predictor and corrector steps.

Wall Points

The governing equations are cast in characteristic form and differenced in the manner proposed by Kentzer.[15] One of these characteristic equations is inadmissible since it carries information from outside the computational domain, and it is replaced by the tangent-flow boundary conditions. The remaining set of equations are written in terms of (α, β, γ) coordinates in which the surface is located along an $\alpha =$ constant coordinate. By defining the appropriate transformation T_3: $(\alpha, \beta, \gamma) \rightarrow (\xi, \eta, \zeta)$, it is possible to apply this set of equations to any of the edges of each zone. At surface points, $\ell n(p)$, $V = \alpha_x v + \alpha_y u$, and s, the entropy, are advanced.

Surface Junctures

Both internal and external junctures are considered; the former has an included angle of <180 deg, whereas the latter has an included angle >180 deg. The general strategy for treating corner points is to define a mapping T_3: $(\alpha, \beta, \gamma) \rightarrow (\xi, \eta, \zeta)$, the inverse of which transforms the intersecting surfaces to $\alpha = 0$. The characteristic relations developed for surface points can then be applied to the corner. In order that the transformation may be nonsingular at the corner, it is necessary to envision the corner as slightly rounded on a subgrid scale. Since the transformation only needs to be evaluated at discrete grid points, the actual corner geometry does not need to be provided, and only the orientation of the $\alpha = 0$ surface at the corner itself needs to be specified. Here it is required that the direction $\alpha_x \boldsymbol{i} + \alpha_y \boldsymbol{j}$ bisect the corner angle in the cross-flow plane.

Shock Points

The current procedure is designed to provide an outer boundary for the computational domain, not to track embedded shocks. Accordingly, shock points are limited to edge 3, and uniform freestream properties are required upstream of the shock. At the shock, flowfield properties, as well as the shock location and slope, are unknown. The correct boundary conditions are provided by the Rankine-Hugoniot relations, which relate the freestream properties, the shock slopes, and the properties behind the shock. An analysis of the characteristics associated with Eqs. (1) indicates that there is one admissible characteristic relation at the shock. This expression, when combined with the Rankine-Hugoniot relations, results in a system of equations to advance c and $c_{\bar{z}}$.

Edges and Surface Discontinuities

As a calculation is marched along a missile axis, new wing or cowl surfaces may appear or disappear as illustrated in Fig. 4. At such locations, the edge-point type changes to reflect the new cross-sectional geometry. A *leading-edge* point occurs at a wall point that in the previous step was an interior point. Conversely, a *trailing-edge* point occurs at an interior point that in the previous step was a wall point. The strategy employed for dealing with surface edges applies a local analysis. This procedure improves accuracy near edges and increases robustness. The edges are located approximately to within the local mesh spacing.

At the leading edge, the computational algorithm proceeds by completing the step in which the leading edge is encountered without taking the new surface into account. The resulting flow properties are then taken as the conditions immediately upstream of the leading edge. A local analysis is applied to determine flow properties immediately downstream of the edge on both sides of the new surface. This analysis is based on the Mach number normal to the leading edge M_n. If $M_n > 1$, an attached shock or expansion occurs in most cases, and the oblique-shock and Prandtl-Meyer relations are applied. In other cases, empirical relations are used to estimate property values at the leading edge. Estimated property values are obtained by defining an effective oblique-shock angle at the leading edge and assigning the streamline direction. This procedure was developed by comparison with experiment and is discussed in Ref. 16.

At the trailing edge, properties on the two sides of a wall surface are coalesced into a single interior point. The computational algorithm proceeds by completing the step in which the trailing edge is encountered without taking the edge into account. The resulting flow properties on the two sides of the surface represent the properties at the trailing edge and serve as upstream conditions for the local analysis. If the flow components normal to the trailing edge on both surfaces are sufficiently supersonic, the steady supersonic Riemann problem solution yields the correct conditions at the coalesced point. To avoid the necessity of solving the Riemann problem, a simpler method has been adopted that turns the streamlines from both surfaces onto the plane of the zone boundary. The coalesced point values are determined by averaging these two sets of conditions. At trailing edges featuring a normal flow component that is subsonic, coalesced property values are determined by averaging adjacent interior point conditions.

At wall surface locations where the slope is discontinuous, a local analysis is also applied. As in the case of the leading edge,

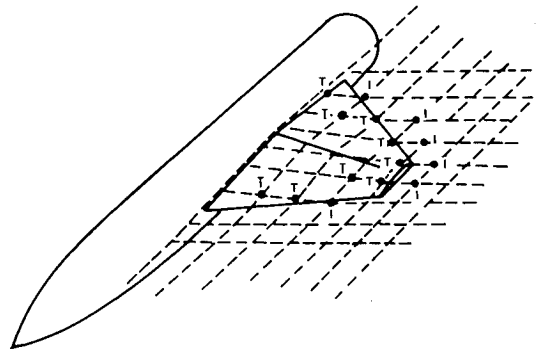

Fig. 4 Surface edge points (T) and interior points (I) adjacent to the surface edges.

this analysis improves resolution downstream of the discontinuity and increases the robustness of the computational procedure. This procedure is implemented by neglecting the change in surface slope until the step in which it has been encountered has been completed. Then the local analysis is applied, which consists of turning the surface streamlines to match the new surface slope, using the shock or expansion relations.

Special Procedures

The presence of surface edges requires the introduction of special procedures for advancing points labeled T and I in Fig. 4. In all cases, modified procedures must be applied at points I, which have two neighboring T points on the upper and lower surfaces of the wing. I points are advanced twice, using each of the neighboring points and, following the corrector step, the two resulting sets of property values are averaged. In situations where strong shocks or expansions are attached to surface edges, differencing near the leading edge is modified in the following fashion:

Alteration of Differences Along Zone Boundaries

Both T and I points are of concern here. At the surface edge a strong shock or Prandtl-Meyer expansion may occur. Under these conditions T points are not affected by I points, and vice versa. This correct domain of dependence can be imposed at point I by applying a one-sided difference along the zone boundary directed away from the surface edge. At point T, this procedure leads to an instability, and differences calculated using points T and I are set to zero.

Normal Surface Derivative Damping at the Leading Edge

Large property jumps can occur at the leading edge due to the existence of a shock or expansion. The surface-normal derivatives at T-type points are unrealistically large, reflecting the fact that the difference is being taken across a discontinuity. Use of calculated normal derivative values in the vicinity of the leading edge leads to an inaccurate solution. More realistic results can be obtained by damping the normal derivatives near the leading edge (i.e., reducing the derivative by an empirically determined corrective factor).

In computations featuring body separation, irregular geometry, and highly swept leading edges, artificial viscosity must often be added. This is accomplished with a switched Shuman filter triggered by a density switch and applied following the corrector step.[12] For interior points, smoothing is applied to the conservation quantities while, at surface points, smoothing is applied to the advanced quantities.

IV. Results

In this section, results are presented for three different configurations. The multiple-zone calculations were performed on a CYBER 170/720 and required $5(10^{-3})$ s/point/step. The mesh size employed for each zone is indicated by $(N \times M)$ where N and M are the number of points in the radial and circumferential directions, respectively. The presented results were achieved using a step size of 90% of the CFL limit, and artificial viscosity was not used. In each of the present calculations, all the zones were referred to the same origin. This allows the procedure discussed in Sec. II to be modified. Metric values at abutting edges were calculated using centered differences of r, ϕ instead of x, y. The illustrated results feature the interior point metrics calculated using central differences. Nearly identical results were obtained using the analytic formulation. The selected mesh for the finned sections of the body was usually the largest that could be fit on the CYBER 170-720. Coarser meshes produced similar surface pressures and forces, along with the expected loss in flowfield resolution.

In Ref. 17, the finned tangent ogive body, shown in Fig. 5, was tested in supersonic flow. The fins featured surface slope discontinuities at various locations along the surface. The freestream Mach number was sufficiently large to allow attached shocks to occur at the fin leading edge in most cases. Numerical results have been compared to experimentally measured surface pressures at Mach 3.7 for a clipped delta configuration in the "plus" roll orientation. Calculations for these cases were made in two runs. A single (15×15) zone was used to advance the solution to an axial station slightly forward of the tail leading edge. The flowfield was then rezoned to two (40×19) zones, shown in Fig. 6, for the computation over the

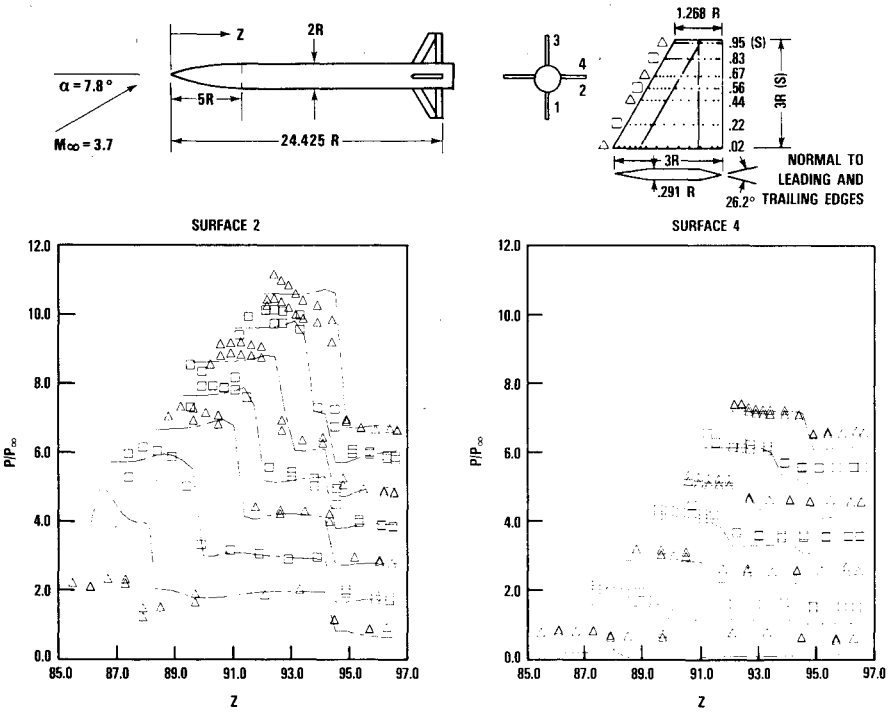

Fig. 5 Calculated and measured[17] fin surface pressures on a clipped delta-fin model. Each successive spanwise curve has its zero reference shifted by 1.

tail surfaces. Calculated and measured fin surface pressures are compared in Fig. 5. Fin surface pressure distribution shows reasonable agreement between calculation and experiment, although problem areas do occur near the body-tail junction and on the trailing-edge panel. Both these areas are strongly influenced by viscous effects, and lack of close agreement is not surprising. The computed flowfield at an axial station near the center of the wing is shown in Fig. 6. Clearly evident is the interaction between shocks generated by the horizontal and lower fin.

Results for a missile with wraparound fins at Mach 2.5 and 3 are presented in Figs. 7–9. The missile geometry is illustrated, along with the measured normal force that was obtained in Ref. 18 on a spinning model. A single (15 × 25) zone was employed forward of the wing, while four (40 × 10) zones were applied over the fins. Mesh clustering in the radial direction was used to increase the number of points in the vicinity of the fins. As indicated in Fig. 7, good agreement is obtained between computed and measured normal force. The calculated center of pressure (not shown) is about a caliber aft of the measured one. The rolling moment, which was measured in

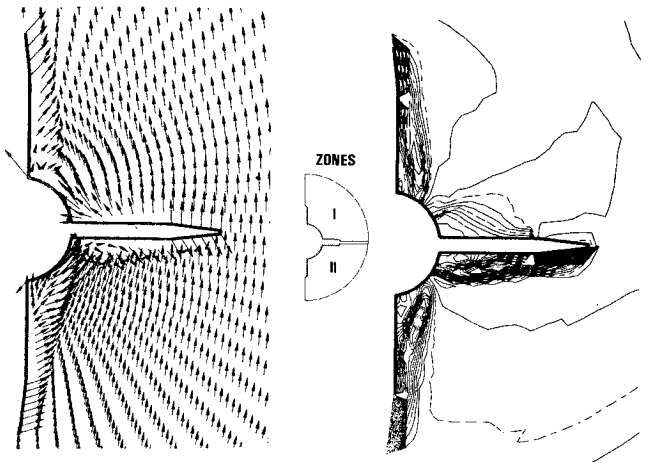

Fig. 6 Calculated cross-flow velocity and pressure for the case depicted in Fig. 5, at station $z = 24.8R$.

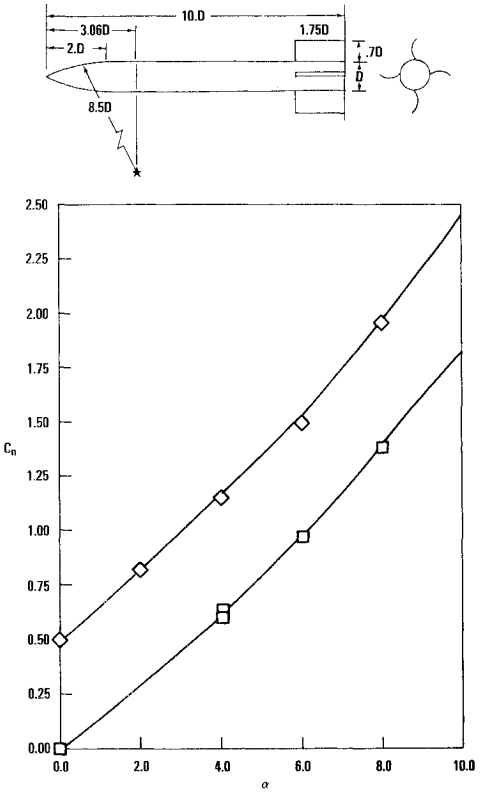

Fig. 7 Calculated and measured[18] normal force on a wraparound fin configuration: □ Mach 2.5, ◇ Mach 3.0. The Mach 2.5 curve is offset by 0.5.

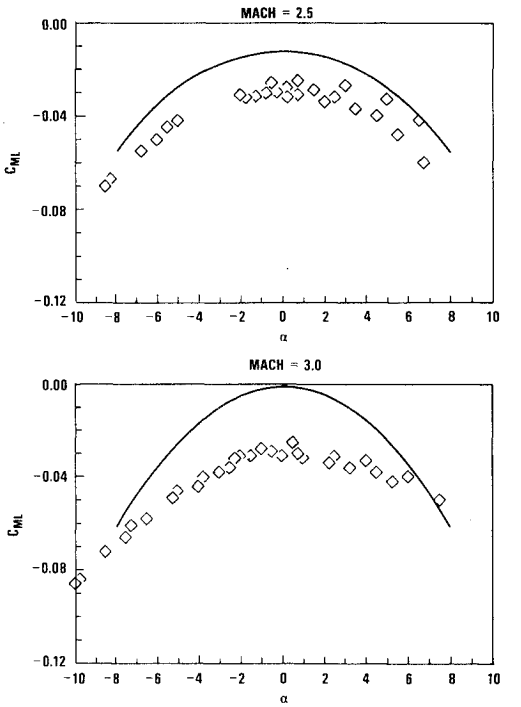

Fig. 8 Calculated and measured[19] roll moment on the wraparound model of Fig. 7. Lines are values; symbols are measured data.

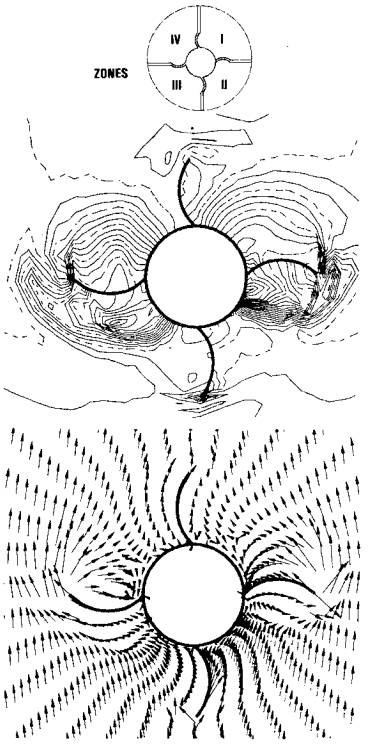

Fig. 9 Calculated cross-flow velocity and pressure at axial station $z = 9.8D$ on the wraparound model of Fig. 8.

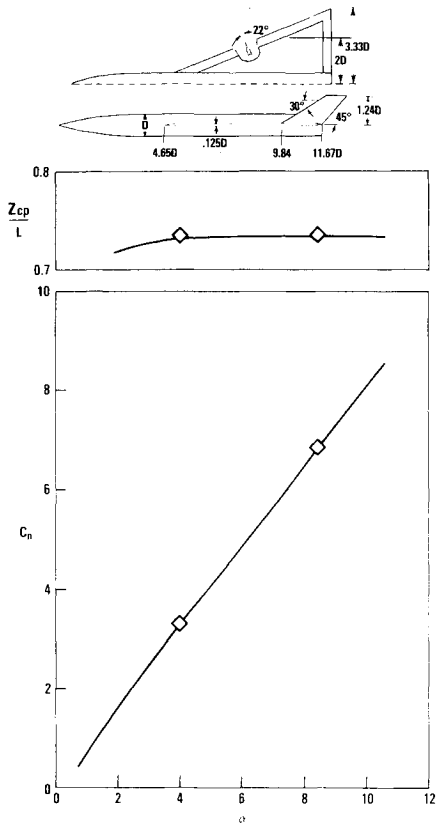

Fig. 10 Calculated and measured[20] normal force and center of pressure on a body-wing-tail configuration.

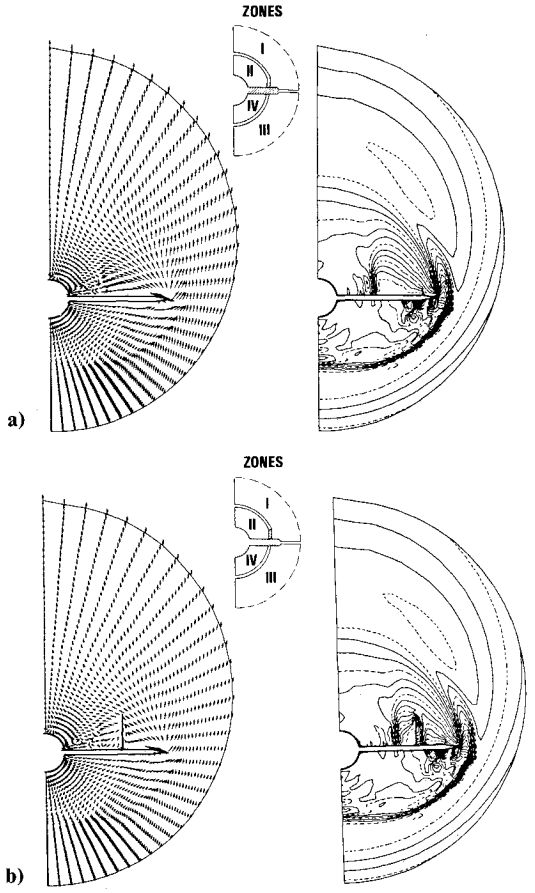

Fig. 11 Calculated cross-flow velocity and pressure on the configuration in Fig. 10: a) without tail, b) with tail at station $z = 11D$.

Ref. 19 and is exhibited in Fig. 8, does not agree closely with calculation at low incident. However, the trend with incidence and Mach number is reproduced. The cross-flow plane in the vicinity of the fins is shown in Fig. 9 at a Mach number of 3 and incidence of 8 deg. The pressure contour plot indicates the presence of a shock under the right horizontal wing that is stronger than that under the left horizontal wing.

A swept-wing configuration with vertical tail located on the wing is shown in Fig. 10. The calculation of this configuration was carried out using a single (18 × 19) zone up to the wing. Two (40 × 19) zones were employed on the wing forward of the tail. Two (30 × 19) and two (15 × 19) zones were employed over the vertical tail section. The tail thickness was neglected in order to simplify the geometry description. The calculated normal force and center of pressure are shown in Fig. 10 and agree well with experiment.[20] Cross-flow velocities and pressures at an axial station slightly forward of the tail are given for this configuration in Fig. 11, along with those for a similar configuration without a vertical tail. The presence of the tail introduces a shock near its outboard surface, followed by an expansion about the tip of the tail. A second shock is visible inboard of the tail surface. In both cases, a detached shock can be seen lying below the wing sections.

V. Concluding Remarks

A multiple-zone computational method has been developed that is capable of treating missile and aircraft configurations. The method features analytically generated meshes in each zone, with a metric smoothing procedure at abutting edges to simplify the zone interfacing. The computational procedure has been applied to several different examples. In general, results are in good agreement with experiment. In addition to being able to treat conventional missile shapes, the multiple-zone procedure is also capable of handling more complex geometries, including aircraft configurations and internal flows.

Acknowledgments

This work was supported by NAVSEA and NAVAIR. The project monitors were Dale Hutchins (AIR-310-C) and Lionel Pasiuk (SEA-62R41). P. Collins also contributed to the project by developing the force integration method.

References

[1]Klopfer, G. H. and Nielsen, J. H., "Euler Solutions for Wing and Wing-Body Combinations at Supersonic Speeds with Leading Edge Separation," AIAA Paper 80-0126, Jan. 1980.

[2]Moretti, G., "Calculation of Three-Dimensional, Inviscid, Supersonic, Steady Flows," Polytechnic Institute of New York, Brooklyn, NY, M/AE Rept. 81-25, Dec. 1981.

[3]Marconi, F. and Salas, M., "Computation of Three Dimensional Flows about Aircraft Configurations," *Computers and Fluids*, Vol. 1, June, 1973, pp. 185–195.

[4]Kutler, P., Reinhardt, W. A., and Warming, R. F., "Multishocked, Three-Dimensional Supersonic Flowfields with Real Gas Effects," *AIAA Journal*, Vol. 11, May 1973, pp. 657–664.

[5]Marconi, F., Salas, M., and Yaeger, L., "Development of a Computer Code for Calculating the Steady Super/Hypersonic Inviscid Flow Around Real Configurations, Vol. I—Computational Techniques," NASA CR-26785, April 1976.

[6]Solomon, J. M., Ciment, M., Ferguson, R. E., and Bell, J. B., "Inviscid Flowfield Calculations for Reentry Vehicles with Control Surfaces," *AIAA Journal*, Vol. 15, Dec. 1977, pp. 1742–1749.

[7]Moretti, G., "Conformal Mappings for Computation of Steady, Three-Dimensional, Supersonic Flows," *Numerical/Lab. Computer Methods in Fluid Dynamics*, ASME, Vol. 13, 1976, pp. 13–28.

[8]Bush, R. H., "External Compression Inlet Prediction Using an Implicit, Upwind, Multiple Zone Approach," AIAA Paper CP 85-1521, 1985.

[9]Buning, P. G. and Steger, J. L., "Graphics and Flow Visualization in Computational Dynamics," AIAA Paper CP 85-155, 1985.

[10]Benek, J. A., Buning, P. G., and Steger, J. L., "A 3-D Chimera Grid Embedding Technique," AIAA Paper CP 85-1523, 1985.

[11]Rai, M. M., "A Conservative Treatment of Zonal Boundaries for Euler Equation Calculations," AIAA Paper 84-0164, 1984.

[12]Wardlaw, A. B., Priolo, F. J., and Solomon, J. M., "An Inviscid Multiple Zone Method for Supersonic Tactical Missiles," NSWC TR 85-484, 1985.

[13]Priolo, F. J., Wardlaw, A. B., Baltakis, F. P., and Solomon, J. M., "Inviscid Multiple Zone Strategy Applied to Complicated Supersonic Tactical Missiles," AIAA Paper 85-1813, 1985.

[14]Priolo, F. J. and Wardlaw, A. B., "An Inviscid Multiple Zone Method for Supersonic Tactical Missiles—User's Manual," NSWC TR 85-486, 1985.

[15]Kentzer, C. P., "Discretization of Boundary Conditions on Moving Discontinuities," *Proceedings of the 2nd International Conference on Numerical Methods in Fluid Dynamics, Lecture Notes in Physics*, Vol. 8, Springer-Verlag, New York, 1971, pp. 108–113.

[16]Wardlaw, A. B., Baltakis, F. P., Solomon, J. M., and Hackerman, L. B., "An Inviscid Computational Method for Tactical Missile Configurations," NSWC/WOL TR 81-457, March 1981.

[17]Lamb, M., Sawyer, W. C., Wassum, D. L., and Babb, C. D., "Pressure Distributions on Three Different Cruciform Aft-Tail Control Surfaces of a Wingless Missile at Mach 1.60, 2.36 and 3.780," NASA TM-80097, Aug. 1979.

[18]Regan, E. J. and Schermerhorn, V. L., "Supersonic Magnus Measurements of the 10-Caliber Army-Navy Spinner Projectile with Wrap-Around Fins," NOLTR 70-211, Oct. 1970.

[19]Dalke, C. W., "A Review and Status of Wrap-Around Fin Aerodynamics," *10th Navy Symposium and Aeroballistics*, Vol. 1, No. 10, July 1975, pp. 279–324.

[20]Lamb, M., Sawyer, W., and Thomas, J., "Experimental and Theoretical Supersonic Lateral-Directional Stability Characteristics of a Simplified Wing-Body Configuration with a Series of Vertical Tail Arrangements," NASA TP-1878, Aug. 1981.